

# STEM-EDX tomography of bimetallic nanoparticles: A methodological investigation



Thomas J.A. Slater<sup>a</sup>, Arne Janssen<sup>a</sup>, Pedro H.C. Camargo<sup>c</sup>, M. Grace Burke<sup>a</sup>,  
Nestor J. Zaluzec<sup>a,b</sup>, Sarah J. Haigh<sup>a,\*</sup>

<sup>a</sup> School of Materials, University of Manchester, Manchester M13 9PL, UK

<sup>b</sup> Nanoscience and Technology Division, Argonne National Laboratory, Argonne, IL 60439, US

<sup>c</sup> Departamento de Química Fundamental, Instituto de Química, Universidade de São Paulo, São Paulo, Brazil

## ARTICLE INFO

### Article history:

Received 11 March 2015

Received in revised form

1 June 2015

Accepted 11 October 2015

Available online 22 October 2015

### Keywords:

Energy dispersive X-ray spectroscopy

Electron tomography

Bimetallic nanoparticles

## ABSTRACT

This paper presents an investigation of the limitations and optimisation of energy dispersive X-ray (EDX) tomography within the scanning transmission electron microscope, focussing on application of the technique to characterising the 3D elemental distribution of bimetallic AgAu nanoparticles. The detector collection efficiency when using a standard tomography holder is characterised using a tomographic data set from a single nanoparticle and compared to a standard low background double tilt holder. Optical depth profiling is used to investigate the angles and origin of detector shadowing as a function of specimen field of view. A novel time-varied acquisition scheme is described to compensate for variations in the intensity of spectrum images at each sample tilt. Finally, the ability of EDX spectrum images to satisfy the projection requirement for nanoparticle samples is discussed, with consideration of the effect of absorption and shadowing variations.

© 2015 The Authors. Published by Elsevier B.V. This is an open access article under the CC BY license (<http://creativecommons.org/licenses/by/4.0/>).

## 1. Introduction

The characterisation of nanoparticles has been greatly enhanced over the past decade by the increasing availability of three-dimensional structural information obtained via electron tomography [1,2]. This technique involves tilting the sample to different angles along one or more axes and collecting a series of images at each tilt angle. This data can be used to reconstruct the three dimensional sample volume via an established tomographic algorithm. Electron tomography reconstructions using tilt series data sets of transmission electron microscope (TEM) or scanning transmission electron microscope (STEM) images have allowed the morphology and distribution of nanoparticles on a substrate to be fully characterised in three dimensions [3–5]. However, obtaining complementary three dimensional elemental information is more difficult. Using electron energy loss spectroscopy (EELS) or energy dispersive X-ray (EDX) spectroscopy in the STEM it is possible to obtain elemental maps that show features down to the atomic scale [6,7]. This two dimensional spectrum imaging, in which a spectrum is collected for every pixel, is now routine but, the combination of spectroscopic imaging with electron tomography has proved far more challenging experimentally. Practically, the

principle limitation when acquiring both EELS and EDX tomographic spectrum image tilt series' are the long acquisition times associated with even a single spectrum image [8].

New EDX detector geometries in the transmission electron microscope are capable of EDX spectrum imaging at a wide range of tilt angles and with a significantly improved solid angle for X-ray collection, greatly increasing the ability to acquire EDX tomography data sets [9,10]. In particular, the Super-X detector configuration, composed of four separate silicon drift detectors (SDDs) arranged symmetrically around the optic axis, has proved capable of performing EDX tomography with much shorter acquisition times at each specimen tilt angle [11,12]. However, even for these new generation large solid angle detectors, the geometrical percentage of X-rays detected is low (approximately 6% for 0.7 sr), such that the signal-to-noise ratio of EDX spectrum images is often poor. The low signal detection means that very high electron doses are often required, through the use of high probe currents and/or long acquisition times. In the tilt series discussed in this work a total dose of approximately  $7 \times 10^9$  electrons/nm<sup>2</sup> was employed, similar to that reported for a previous study of a single transistor published by Lepinay et al. [12]. This will often limit the application of the technique, as many nanoparticles are insufficiently robust to withstand this high total dose without significant structural change. An important aim of experimental procedures in EDX tomography should therefore be to limit the overall electron dose whilst maximising the signal at each angle.

\* Corresponding author.

E-mail address: [sarah.haigh@manchester.ac.uk](mailto:sarah.haigh@manchester.ac.uk) (S.J. Haigh).

Limiting the number of projections to as few as possible has the advantage of improving the quality of the spectrum image data for each tilt angle and is therefore highly desirable, although requiring the use of advanced reconstruction algorithms [13,14] to realise high fidelity reconstruction when few projections are used.

Historically, one of the key challenges for EDX tomography has been that traditional single detector EDX systems are often limited to a very narrow range of tilt angles [8]. At other angles the penumbra of the specimen holder prevents an X-ray signal being detected by ‘shadowing’ the EDX detector [8]. The design of new detector geometries such as the Super-X detector system [15] means that X-rays may be detected for a wider range of specimen tilt angles ( $\pm 70^\circ$ ), although some detector shadowing does occur for samples that are deposited on standard TEM grids or that use traditional high-tilt tomography holders [16]. Shadowing at all tilt angles is only eliminated through the use of  $360^\circ$  rotation tomography holders [12] and these are not compatible with all types of specimen. Shadowing of X-ray detectors will cause intensity variations as a function of tilt angle and will lead to systematic errors in the intensity contribution to the final reconstruction. Consequently, it is desirable for shadowing-induced intensity variations to be corrected either as part of the acquisition procedure or by post processing.

This paper investigates a novel methodology for EDX tomography of isolated nanoparticles. As an example we have used AgAu nanoparticles for which EDX tomography has already been demonstrated to give important insights into the different elemental distributions as a function of overall composition [17]. The details of detector shadowing are investigated and a varied-time acquisition scheme is introduced to compensate changes in detector solid angle. Finally, the ability of EDX spectra to satisfy the projection requirement for nanoparticle samples is discussed, with reference to absorption and shadowing variation across a sample.

## 2. Experimental methods

High angle annular dark field (HAADF) scanning transmission electron microscope imaging was performed on an FEI probe-corrected Titan G2 80–200 S/TEM with a high brightness X-FEG electron source and Super-X energy dispersive silicon drift detectors (SDDs). The microscope was operated at an accelerating voltage of 200 kV with a beam current of 0.5 nA, a convergence angle of 21 mrad and a HAADF acceptance inner angle of 50 mrad. EDX spectrum images were acquired in the Bruker Esprit software using the Titan’s Super-X detector system with a dwell time of 30  $\mu$ s and a typical image size of  $512 \times 512$  pixels. This detector has a total solid angle of approximately 0.7 sr distributed over four  $30 \text{ mm}^2$  SDDs equally separated at  $45^\circ$  from the holder tilt axis at an elevation angle of approximately  $18^\circ$  from the horizontal [15]

(Fig. 1). Full spectrum image datacubes were exported from Esprit to Gatan’s DigitalMicrograph software. As individual pixels were too noisy for accurate quantitative analysis, elemental X-ray counts for each tilt angle were extracted from spectra obtained from a summation over all pixels in the full spectrum image. Background subtraction was performed via a window method using energy windows (of the same width as that of the signal window) before and after the peaks of interest, taking care to ensure that no other peaks are included in these regions [18]. Elemental maps were extracted at energies of 2.92–3.06 keV (Ag L $\alpha$ ) and 9.58–9.82 keV (Au L $\alpha$ ) and are shown after applying a 5-pixel smoothing (as detailed in Section 3.2).

A Fischione 2020 single tilt tomography holder was compared to an FEI high-visibility low-background double-tilt specimen holder. EDX tomography used an angular increment of  $10^\circ$  and a tilt range of  $\pm 70^\circ$ . Traditional tilt series data sets were obtained with a constant acquisition time of 300 s for each spectrum image, while in our novel time-varied tomographic scheme acquisition times were varied between 236 s and 895 s in order to compensate for the calibrated detector shadowing at the particular specimen tilt. Manual alignment was used to centre the specimen at each tilt angle and HAADF images were acquired simultaneously with spectrum images at each tilt angle. Additional intermediate HAADF images were collected every  $5^\circ$  to assist with subsequent alignment of the data set via cross-correlation of HAADF images. Spatial image alignment was performed using cross-correlation of HAADF images in FEI’s Inspect3D software package. Tilt axis alignment was also undertaken in Inspect3D followed by using a simultaneous iterative reconstruction technique (SIRT) to perform the reconstruction with 20 iterations. ImageJ [19] and FEI’s Avizo software platforms were used for visualisation of reconstructions.

To investigate the effect of variable intensity data sets a phantom was simulated in MATLAB software consisting of a simple three-phase image; an 8-bit image of a circle (signal intensity=193) surrounded by a ring (signal intensity=253) on a background of intensity 1. The Radon function was used to simulate projections between  $\pm 70^\circ$  at  $10^\circ$  intervals. The inverse Radon function was then used to perform a filtered backprojection, firstly, on projections of the same intensity and, subsequently, with projections multiplied by the same factor as the intensity differences provided by shadowing from a single tilt tomography holder on all four Super-X detectors (Fig. 2c), as well as multiplication factors taken from the variation in intensity from only two Super-X detectors (Fig. 2b).

Three-dimensional optical images of the Fischione 2020 holder were acquired with a Keyence VK-X210 3D laser scanning confocal microscope. The microscope is equipped with a violet laser (wavelength 408 nm) and a 16-bit photomultiplier for accurate detection of reflected light on surfaces. High-resolution three-dimensional (3D) maps of the top and bottom surfaces of the holder

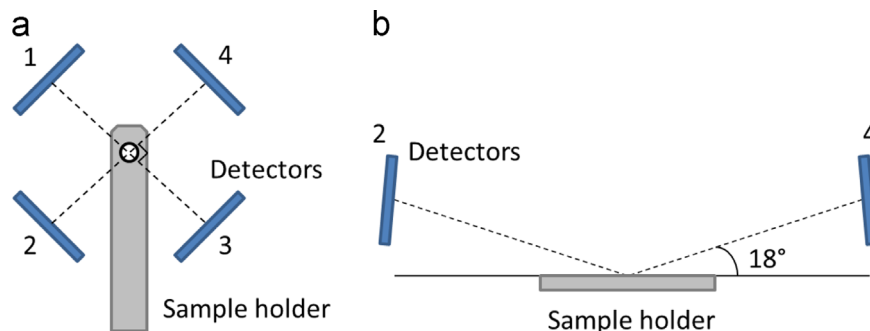


**Fig. 1.** Schematic illustrating the geometry of the Super-X detectors in the FEI Titan G2 80–200 (S) TEM. (a) viewed in the direction of the electron beam and (b) viewed for a 2D cross-section passing through detectors 2 and 4 at  $45^\circ$  to the long axis of the specimen holder. Detectors are labelled 1–4 as used in FEI TIA software.

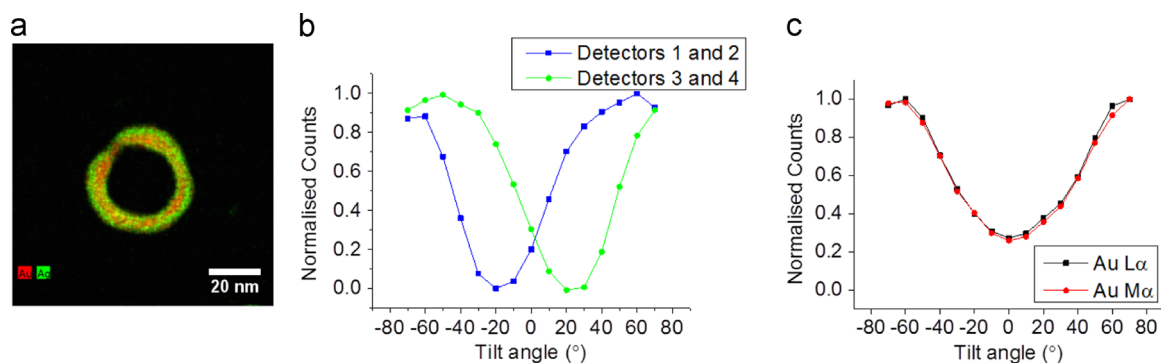


**Fig. 2.** Calibration of Super-X detector shadowing in the Titan G2 for the Fischione 2020 single tilt tomography holder. (a) EDX Au and Ag elemental map for a single AgAu nanoparticle at 0° showing the particle that was used to perform the detector shadowing calibration, (b) background subtracted Au L $\alpha$  X-ray counts (9.7 keV) at each pair of detectors as a function of tilt angle, taken from EDX spectrum images acquired for the same AgAu nanoparticle using an acquisition time of 5 mins, 10° tilt increments and an angular range of  $\pm 70^\circ$  and (c) background-subtracted summed X-ray counts for Au L $\alpha$  (9.7 keV) and Au M $\alpha$  (2.1 keV) peaks.

were obtained by stitching 54 single images of the top side and 25 single images of the bottom side together. The assembled three-dimensional map of each surface was analysed with the Keyence VK Analyser Software package.

AgAu nanoparticles were chosen as a suitable test system for this study because of their robustness to the structural changes induced by the electron beam and from the presence of two elements with characteristic X-rays in different parts of the X-ray spectrum. These particles were synthesised via a galvanic replacement reaction between Ag nanoparticles and AuCl $_4$ (aq), as detailed in previous work [20]. This process leads to nanoparticles with a range of morphologies including hollow donut-like structures like that shown in Fig. 2a. At Au contents less than approximately 20 at% the gold is segregated to the nanoparticle surface while at higher Au contents the nanoparticle surface is enriched in Ag. A nanoparticle sample of average composition Ag 78 at% Au 22 at%, as measured by flame absorption spectroscopy, was deposited from solution onto continuous carbon-coated copper 200-mesh TEM grids (from Agar Scientific, product code AGS160). Care was taken to acquire tilt-series of nanoparticles in the centre of the grid squares.

### 3. Results and discussion

#### 3.1. Calibration of detector shadowing

In order to account for detector shadowing, when using a standard tomography holder, the extent of shadowing at each angle must first be accurately calibrated. Doing this requires a sample that will itself give a constant X-ray signal independent of tilt angle. Robust single nanoparticles like that shown in Fig. 2a present a suitable specimen from which X-ray counts associated with the elements present within the nanoparticles should not significantly vary with specimen tilt angle. Any variations in X-ray peak intensity from spectral images of single nanoparticles should be due to detector shadowing alone.

In order to characterise the variation in total X-ray count rates as a function of tilt angle, spectrum images were acquired with a Fischione 2020 single-tilt tomography holder using the Titan's Super-X EDX detector system (Fig. 1) for a single AgAu nanoparticle. Spectrum images were acquired for 5 min every 10° for a tilt range of  $\pm 70^\circ$  (Fig. 2b and c). Detectors mounted on either side of the holder tilt axis will show similar behaviour and the response of detectors 3+4 is symmetrical to that of detectors 1+2 (Fig. 2b). The response of these pairs of detectors is similar to that of a standard geometry single SDD detector [16]. The full detector response (Fig. 2c) consists of the sum of detectors 1–4. Perhaps

surprisingly, this data demonstrates that for this specimen holder the poorest X-ray detection efficiency occurs at low specimen tilts. At 0° the Super-X detector collects only 30% of the X-rays measured at a specimen tilt of 60° for the same nanoparticle, due to the penumbra of the Fischione 2020 tomography holder. The Au L $\alpha$  (9.7 keV) and Au M $\alpha$  (2.1 keV) characteristic X-ray peaks are found to display an almost identical relationship with specimen tilt angle (Fig. 2c), demonstrating that detector shadowing does not vary with X-ray energy for this energy range. This suggests that the same compensation of shadowing can be used for all characteristic X-ray peaks above 2.1 keV.

Shadowing of the X-ray detectors is possibly due to either the penumbra of the sample holder or the bars of the copper TEM grid, or a combination of both on different sides of the holder. In order to determine the source of shadowing, and the angles at which X-rays are shadowed in tilt series, we have taken an optical profile of the top and bottom surfaces of the 2020 holder. A three dimensional image of the surface of the Fischione holder is produced (Fig. 3a and c), in which line profiles of height variations of the holder give the angles at which the holder shadows any emitted X-rays. The detectors are located at 45° angles azimuthally from the tilt axis (Fig. 1a) and therefore we have extracted line profiles at an azimuthal angle of 45° from both sides (Fig. 3b and d). Initially we assume the nanoparticle specimen is located on the carbon film in the centre of a grid square in the middle of the holder. We also assume that the carbon film of the grid lies flat on top of the grid, the square holes have a width of 90  $\mu$ m, the grid bar height is 20  $\mu$ m and the grid is oriented at 45° to the tilt axis. We neglect bowing of the carbon film; a phenomenon which is known to occur for a number of different grids from a range of suppliers and which may increase with the large dose supplied to the area surrounding the nanoparticle. The line profiles in Fig. 3 reveal a polar angle of 21° from the specimen to the top surface of the holder and 18° to the bottom surface. In comparison, the 200 mesh copper TEM support will provide no shadowing above the sample and shadowing up to an elevation angle of 24° below the sample. Thus for the somewhat idealised situation described above, shadowing above the sample occurs at a polar angle of 21° due to the sample holder and shadowing below the sample occurs at a polar angle of 24° due to the grid bars (Fig. 4). Use of these angles for shadowing assumes point detectors at 45° azimuthal angles to the tilt axis, but we note that this is an approximation as the finite detector size will cause shadowing to vary over the width of the detector.

The angle intersected by each detector can be calculated through prior knowledge of the total solid angle and the detector areas. Given the Super-X detector system is characterised by a total solid angle of approximately 0.7 sr and a single detector area of

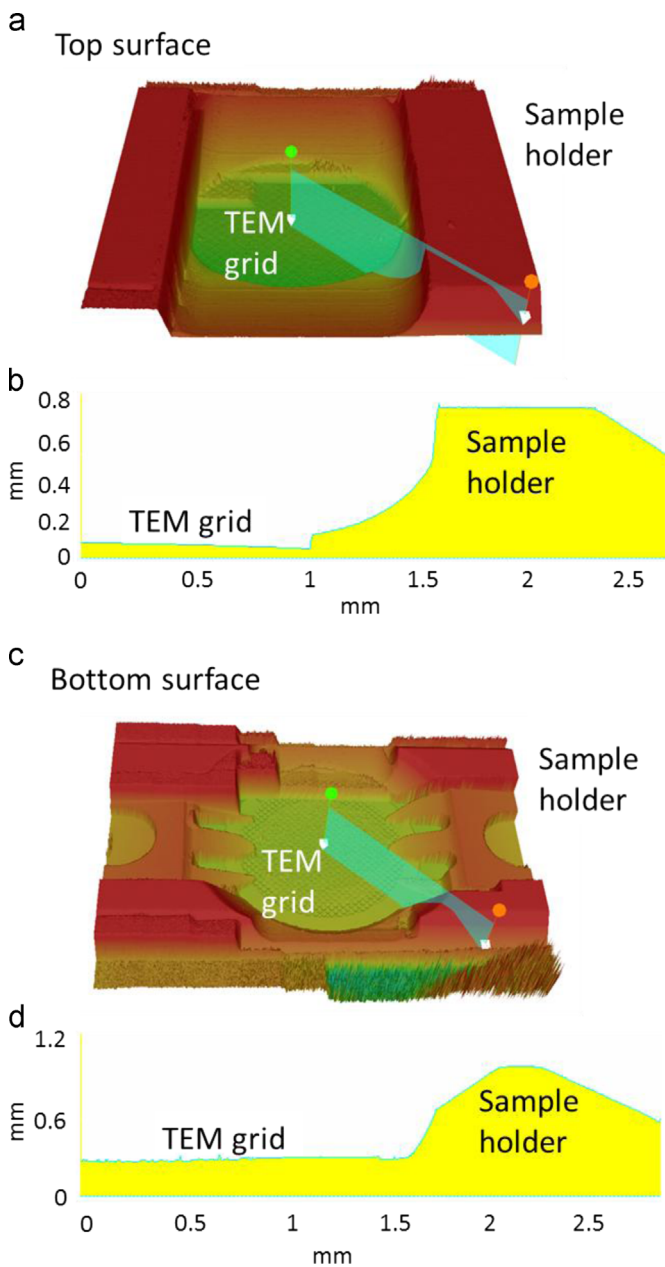


**Fig. 3.** Optical profiles of the top and bottom surfaces of the Fischione 2020 holder. (a) 3D profile of the top surface of the holder with the direction of line profile b, illustrated. (b) Line profile of plane indicated in a, displaying a polar angle of approximately  $21^\circ$  from the centre of the grid to the highest point of the top surface of the holder. (c) 3D profile of the bottom surface of the holder with line profile d illustrated. (d) Line profile of plane indicated in c, from which a polar angle of approximately  $18^\circ$  from the centre of the grid to the bottom surface of the holder is found.

$30 \text{ mm}^2$ , the distance of the detectors from the optic axis is calculated from simple geometry as approximately  $12 \text{ mm}$ . Zaluzec's equation for solid angle determination [21] is:

$$\Omega = 2\pi \left[ \frac{(r_a^2 + d^2 - d\sqrt{r_a^2 + d^2})}{r_a^2 + d^2} \right], \quad (1)$$

where  $r_a$  is the radius of a single detector and  $d$  is the radial distance of the detector from the area of interest. Eq. (1) can be used to estimate the distance from the sample to the detector and therefore allows determination of the polar angle between the

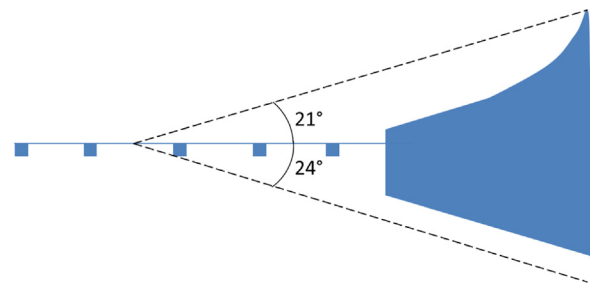


**Fig. 4.** Schematic diagram showing the elevation angles from the sample at which the holder and grid bars will shadow emitted X-rays above and below the specimen in the direction of a single Super-X detector ( $45^\circ$  azimuthal angle).

uppermost and lowermost parts of the detector. This polar angle is approximately  $27^\circ$  in this case, although this neglects detector tilt which is known to be present and which means that the angular extent of the detector is not equal when considering the polar and azimuthal subtending angles. We have determined the elevation angle of the detector using the minimum in X-ray counts observed for our tilt series. Fitting Gaussians to the data in Fig. 2b gives minimum counts at an average  $\alpha$ -tilt of  $18^\circ$  for each pair of detectors. A polar angle,  $\theta$ , in the plane of the detectors, can be translated to a polar angle,  $\alpha$ , in the plane normal (perpendicular) to the  $\alpha$ -tilt axis by the equation:

$$\alpha = \tan^{-1} \frac{\tan\theta}{\cos 45^\circ}. \quad (2)$$

Thus where  $\theta = 27^\circ$ ,  $\alpha = 36^\circ$  and given the elevation angle of the centre of the detector normal to the  $\alpha$ -tilt axis is  $18^\circ$  this predicts that the detector subtends an angle from  $\alpha = 0^\circ$  to  $\alpha = 36^\circ$ . This suggests that each pair of detectors should be fully shadowed when the sample holder is tilted to the angular range of  $\pm 8^\circ$  to  $\pm 32^\circ$  (given the holder shadowing shown in Fig. 4 and converting the  $\theta$  angles ( $21^\circ$  and  $24^\circ$ ) to  $\alpha$  angles in the detector plane ( $28^\circ$  and  $32^\circ$ )). These values appear to qualitatively fit the tilt-series data corresponding to normalised detector counts of less than 10%.

The tilt series data is also compared to the detector shadowing model proposed by Yeoh et al. [22] (Fig. 5a). We have used a value of  $\delta = 5^\circ$  for the detector tilt angle and values of  $d = 10.5 \text{ mm}$  and  $r = 2.9 \text{ mm}$  for the distance to the detector and the radius of the detectors respectively. The data here fits best with their proposed model, for the shadowing angles we have determined, when a detector elevation angle of  $16^\circ$  is used (Fig. 5a). The counts at negative tilt angles appear to fit well qualitatively to the detector model, although the counts at positive tilt angles do not. This may be due to a discrepancy between the detection efficiencies of the two detector pairs. This model also allows consideration of the effect of analysing a nanoparticle away from the centre of a grid square as shown in Fig. 5. If the nanoparticle is away from the centre of the grid square the tilt series becomes asymmetric, although not in the same manner as the data acquired, with the counts of tilts in one direction raised whilst the counts of tilts in the other direction are lowered.

A tilt series of a similar AgAu nanoparticle using an FEI high-visibility low-background double-tilt holder was also acquired for comparison of shadowing using a standard specimen holder (Fig. 6). In comparison, the non-tomographic holder displays the reversed dependence on tilt angle, i.e. low tilt angles give the least detector shadowing over the full tilt range of this holder ( $\pm 30^\circ$ ). This is due to the low-profile of the top of the holder that is designed specifically not to shadow the Super-X detectors and is consistent with similar measurements [23]. Whilst this holder displays a lower variation in counts around  $0^\circ$  tilt, its limited tilt range ( $\pm 30^\circ$ ) would lead to large missing wedge artefacts if it were used for tomographic reconstructions.

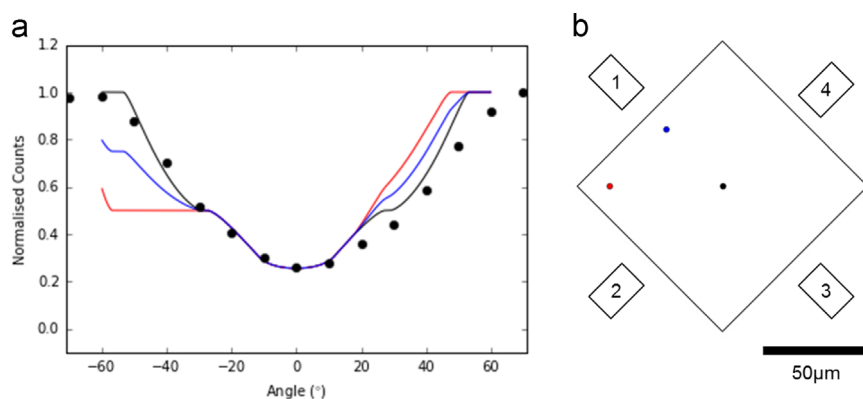


**Fig. 5.** Modelling detector shadowing using the model of Yeoh et al. [22]. (a) Plot of normalised counts with respect to tilt angle for the positions within a grid square indicated in (b). Experimental data points for Au  $L\alpha$  (9.7 keV) X-rays (reproduced from Fig. 2c) are also shown (black dots) for reference. (b) Diagram indicating nanoparticle position within a  $90\ \mu\text{m} \times 90\ \mu\text{m}$  grid square with black in the centre, blue  $10\ \mu\text{m}$  from the edge towards detector 1 and  $45\ \mu\text{m}$  from the edge towards detector 2 and red  $10\ \mu\text{m}$  from both edges towards detector 1 and detector 2. (For interpretation of the references to color in this figure legend, the reader is referred to the web version of this article.).

### 3.2. Considering the effect of uncompensated detector shadowing on tomographic reconstruction

Variations in the intensity of different projections at different tilt angles can lead to artefacts within tomographic reconstructions [24]. This is demonstrated in Fig. 7 for reconstruction of a simulated two-phase object. Fig. 7b shows the object reconstructed using 15 simulated projections each with the same total intensity ( $10^\circ$  tilt intervals over an angular range of  $\pm 70^\circ$ ). In comparison, Fig. 7c shows the same object reconstructed from projections where the total intensity varies in a similar way to that predicted by the shadowing variations revealed in Fig. 2c for the 2020 single-tilt tomography holder, when used with the Super-X detector system. To further illustrate the effect, the projections were backprojected with intensity variations following those of only one pair of Super-X detectors (1+2) (Fig. 7d), as calibrated in Fig. 2b. This illustrates the effect of using a conventional single side-mounted EDX detector. All reconstructions show streaking artefacts associated with a missing wedge of projections and large angular intervals respectively, causing the spherical phantom to become “lemon-shaped” (with “lumps” in the direction of the missing wedge). However, the varied intensity reconstructions also show noticeable variations in intensity, where the intensity of the outer ring is diminished in the plane of the projections with lower intensity (as indicated by the white arrows in Fig. 7b and c). When considering this effect in Fourier space, it can be thought of as weighting more strongly features in central slices away from the slice at  $k_z=0$  (as represented in Fig. 7e and f), thus reducing contrast for features in the central slices around that at  $k_z=0$ .

Where there is sufficient signal within the shadowed regions, these artefacts can be avoided by compensating for the variation in intensity due to shadowing.

### 3.3. Methods for compensating detector shadowing

We propose two methods by which the shadowing of the Super-X detector system can be compensated and variations in the count rates at each specimen tilt angle can be reduced. The first is to acquire spectrum images for a constant time at each tilt angle and then multiply each spectrum image by a ‘shadowing compensation’ factor that normalises the total counts, as suggested in the early work of Möbus [8]. This is straightforward for samples in which the total counts do not change with specimen tilt, such as single nanoparticles, but for samples in which the total counts change with tilt angle, such as thin films, a calibration sample would be needed. The other drawback of this approach is that the signal-to-noise ratio across projections will vary and simply multiplying the lowest intensity projections, or alternatively scaling down the highest intensities, will retain the low signal-to-noise ratios that are present for these projections. Therefore, although this approach has the advantage of simplicity, it will not present the most accurate acquisition scheme. An alternative is to adjust the acquisition time at each tilt angle so as to achieve a constant total specimen X-ray signal for each projection. This allows the maximum tolerable electron dose to be optimally distributed over all projections or can be used to minimise total acquisition time. The disadvantage of this approach is that it requires prior knowledge of the detector shadowing for a particular sample

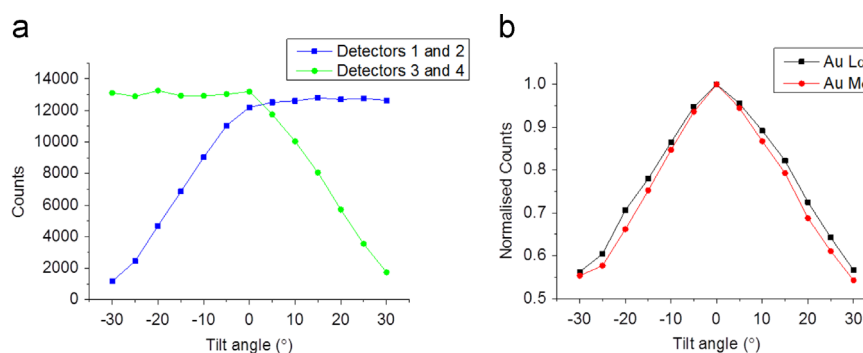


**Fig. 6.** Calibration of Super-X detector shadowing in the Titan G2 for the FEI high-visibility low-background double tilt holder using a similar particle to that shown in Fig. 2a. (a) Au  $L\alpha$  counts at each pair of detectors as a function of tilt angle, (b) background-subtracted Au  $L\alpha$  (9.7 keV) and Au  $M\alpha$  (2.1 keV) X-ray counts extracted from EDX spectrum images acquired for the same AgAu nanoparticle using an acquisition time of 5 mins and  $5^\circ$  tilt increments for angles of  $\pm 30^\circ$ .

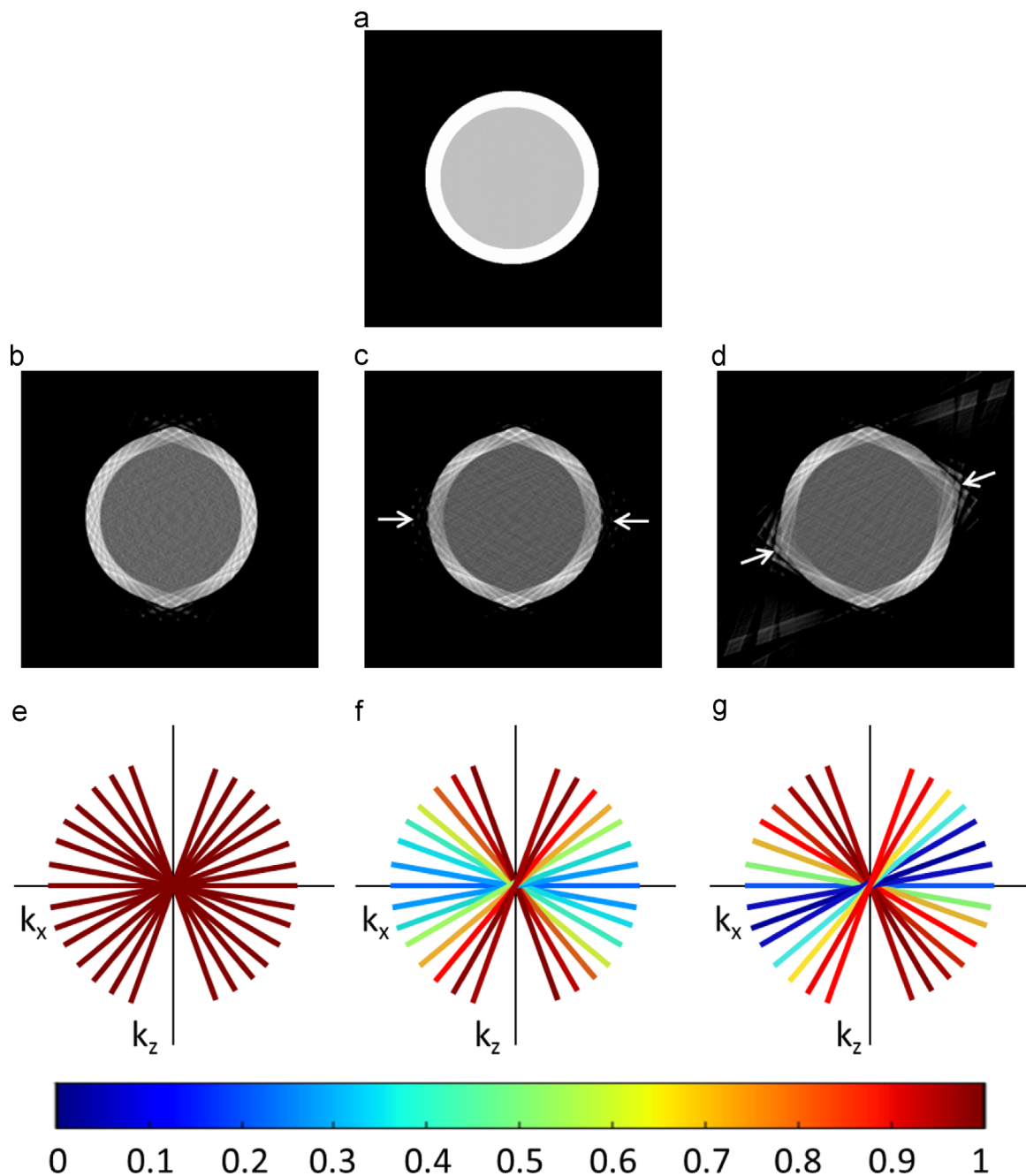


**Fig. 7.** Demonstration of artefacts associated with variations in projection intensities. (a) Simulated two-phase object to be reconstructed. (b–d) Phantom images reconstructed from 15 simulated projections of the two phase image in (a) for a tilt range of  $\pm 70^\circ$  and angular intervals of  $10^\circ$ . (b) Reconstruction using projections of the same intensity, displaying missing wedge and streaking artefacts only. (c) Reconstruction applying the intensity variations due to shadowing (measured when employing all 4 Super-X detectors with a single tilt tomography holder, as shown in Fig. 2c). (d) Reconstruction applying the intensity variations from only a pair of Super-X detectors on one axis, as shown in Fig. 2b. (e–g) Representation in Fourier space of the projections used to reconstruct the images in (b–d) respectively. (e) Constant intensity projections. (f) Variable intensity projections weighted for the full Super-X detector geometry. (g) Variable intensity projections weighted for one pair of Super-X detectors.

holder and microscope combination: obtained using a separate tomographic data set. This calibration can be obtained either by measuring the time taken to acquire a fixed number of X-ray counts for a specific peak within summed spectrum images at each tilt angle or by comparing the different X-ray signals for summed spectrum images obtained with a constant acquisition time as a function of holder tilt (as illustrated in Figs. 2 and 4). We note that as different sample holders have different geometries and as there are variations in the position of EDX detectors on different instruments, calibration of the detector shadowing will need to be performed for each sample holder and microscope combination in order to derive specific time varied acquisition schemes. This

calibration will also differ for different positions within a grid square, as illustrated in Fig. 5, so the accurate position within the grid square should be tracked.

We have acquired EDX spectrum images every  $10^\circ$  using variable tilt-dependent acquisition times as shown in Fig. 8a. The Au  $L\alpha$ , Au  $M\alpha$  and Ag  $L\alpha$  specimen X-ray counts displayed far smaller variations than for a fixed-time acquisition scheme for the whole range of specimen tilt angles (intensity variations were within  $\pm 15\%$ ) demonstrating the success of our time-dependent acquisition scheme for reducing variations in X-ray signals (Fig. 8b). However, even these remaining small variations in summed X-ray counts are larger than can be explained by statistical noise

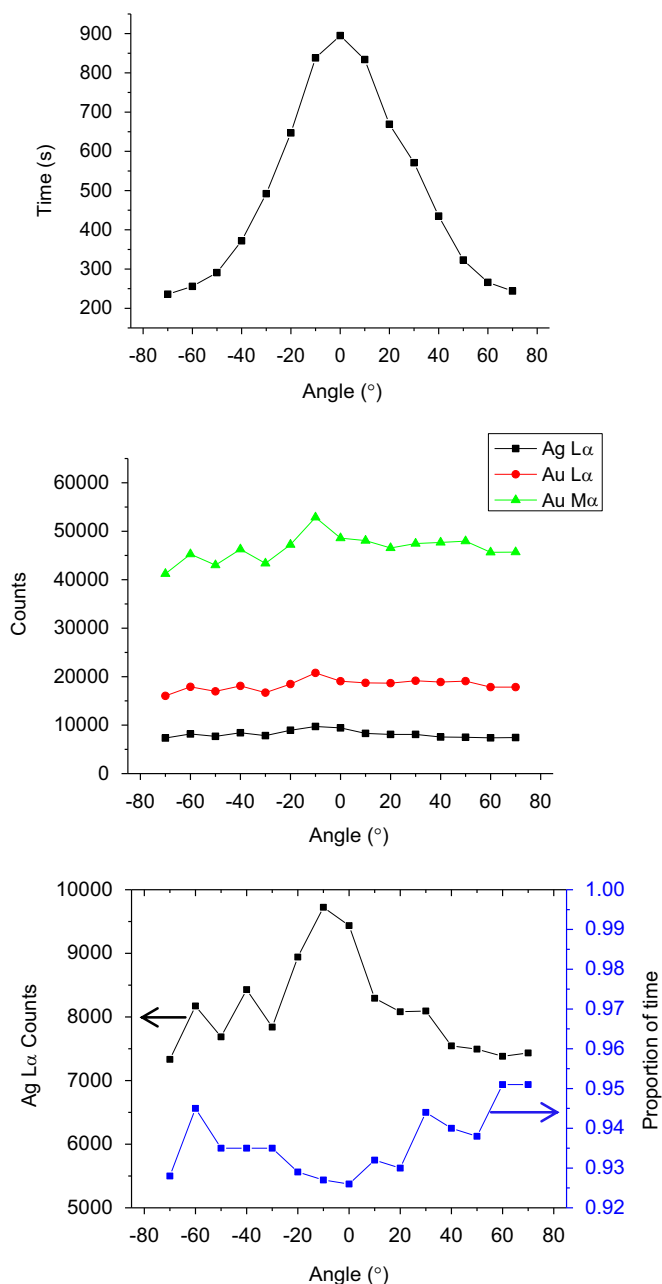


**Fig. 8.** (a) Total acquisition time at each angle employed in the time-varied acquisition scheme reported in this study. (b) Au L $\alpha$ , Au M $\alpha$  and Ag L $\alpha$  X-ray counts at each specimen tilt angle under the varied acquisition time scheme. The variation in counts of each elemental peak using the time-varied acquisition scheme are significantly reduced (variation  $< \pm 15\%$ ). (c) Comparison of Ag L $\alpha$  counts at each specimen tilt angle to the proportion of the calibrated time the acquisition actually took.

fluctuations alone and could be caused by two possible effects. The pixel dwell time and spectrum image size are constant for all tilt angles and this dictates the time increment to which the acquisition time can be specified for each tilt angle. For example, a dwell time of 30  $\mu\text{s}$  and an image size of 512  $\times$  512 pixels results in a discrete minimum time increment of 8 s. Small variations in the X-ray counts are therefore likely to be due to the discrete time increments enforced in the data acquisition. Proportionally, this will have the largest effect for spectrum images acquired with the shortest acquisition times, so for our data will cause the greatest errors at high tilt angles. The accuracy of the shadowing calibration will also affect the accuracy of the X-ray count rates obtained

in the time-dependent data series. Low X-ray signals in the initial fixed time data are likely to cause larger errors when predicting optimal acquisition times. For our holder-microscope combination the spectrum images around 0° tilt have the lowest X-ray signals (approximately 6000 total Au-L $\alpha$  counts at 0° tilt compared to approximately 19,000 counts at 70°). Our calibration shows the largest deviation at small tilt angles (especially at  $-10^\circ$  as shown in Fig. 8b and c), this latter effect is likely to be the more significant for our data. We also note that for very high count rates the ratios of pixel dwell time to detector processing time and count rate can result in lost data, thus also potentially contributing to this variability. The combination of dwell time (approximately a few tens of  $\mu\text{s}$ ), detector time constant (approximately 2  $\mu\text{s}$ ) and count rates ( $< 10$  Kcps) in our experiments did not reach this regime.

The accuracy of the shadowing calibration is poorer where the collection efficiency is low. This accuracy could be improved by repeating the calibration using longer acquisition times or by measuring the time required to reach a certain value of specimen X-ray counts.

### 3.4. Post-acquisition alignment and filtering of EDX tomography data

The choice of tilt increment for the EDX tilt series data set is a compromise determined by factors such as sample stability, achievable tilt range and X-ray count rates. For a fixed tolerable electron dose, larger tilt increments, such as 10°, allow longer acquisition times for each specimen tilt angle, resulting in improved signal-to-noise ratios within the individual spectrum images. However, large tilt increments have been shown to limit the fidelity of tomographic reconstructions when using standard reconstruction algorithms such as the simultaneous iterative reconstruction technique (SIRT) [13,25]. The use of advanced reconstruction algorithms may allow high fidelity reconstructions even when using large tilt intervals of 10° or more [13], but this then poses a problem in the alignment of tilt series'. Alignment procedures based on cross-correlation are less accurate when aligning images taken every 10° than for smaller tilt intervals due to the larger differences between subsequent images [26]. Difficulties with alignment of low signal-to-noise ratio spectrum images can be overcome by performing image registration using the simultaneously acquired HAADF images and subsequently applying this registration data to the elemental maps. Supplementary HAADF images can be acquired at smaller tilt increments to aid registration without significantly increasing the total acquisition time for the data set. To aid alignment we have acquired HAADF images at every 5° to assist in the alignment of EDX maps acquired at every 10°.

The majority of EDX tomography studies have employed smoothing functions to the obtained elemental maps to partially compensate for low signal intensity and a poor signal-to-noise ratio [11,12]. To investigate the effect of smoothing filters on EDX elemental maps it is desirable to work with a simulated data set. In this work we have simulated EDX maps using a test object consisting of a pair of concentric rings; representing a hollow two-phase nanoparticle with the outer phase having a higher concentration of the element being mapped (Fig. 9a(i)). To match the signal to that observed in typical experimental data, the intensity of the image was set to zero for 30% of pixels selected at random from the whole field of view. An equivalent proportion of zero value pixels are typically observed in experimental Au L $\alpha$  elemental maps acquired over 300 s for the nanoparticles used in this study (Fig. 9c). Noise was then added, equivalent to 20 counts per 100  $\times$  100 pixels, producing a simulated EDX map (Fig. 9a(ii)) which provides a good match to the experimental data shown in Fig. 9c. A 5-pixel smoothing window (Fig. 9a(iii)) is shown to suppress noise and give a signal which closely resembles the

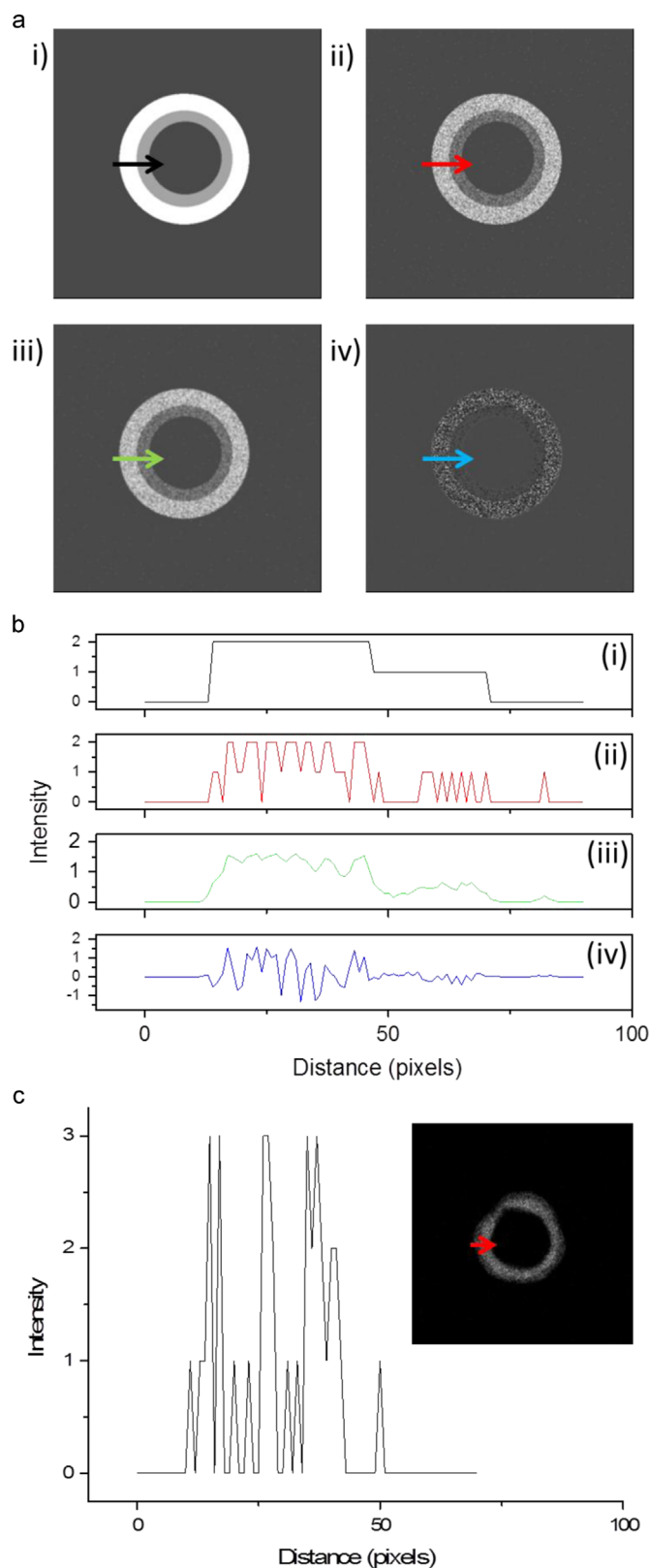


**Fig. 9.** Producing a simulated EDX elemental map which closely resembles the experimental data. (a) (i) Initial test image of object representing a two phase nanoparticle. (ii) Simulated elemental maps in which 30% of data points have been set to zero and Poisson noise added. (iii) Image b processed with 5-pixel smoothing window showing effective suppression of noise in the image. (iv) Image b processed with an edge preserving filter demonstrating the appearance of negative intensity artefacts within the nanoparticle. All images are shown with the same intensity scale and are  $512 \times 512$  pixels. (b) Line profiles (i–iv) through the images (a(i–iv)) respectively at the positions indicated by the arrows. (c) Line profile taken from representative experimental dataset with the corresponding Au L $\alpha$  map of an AgAu nanoparticle shown inset.

original test object. Lepinay et al. report that an edge-preserving smoothing filter suppressed noise well for their test images [12]. However, using this filter on our test image we have found no significant improvement from a generalised smoothing filter and also the production of negative intensity artefacts (Fig. 9a(iv) and b (iv)). We have therefore employed a 5-pixel smoothing to the experimentally acquired Ag and Au elemental maps.

We note that the signal-to-noise ratio for individual spectra can be improved by binning spectral images or acquiring smaller-sized spectrum images at lower magnification. This has the advantage that each pixel contains a more reliable spectrum that can undergo background subtraction and may also assist with other spectral processing procedures such as multivariate statistical analysis (MSA) [27,28]. The disadvantage is that binning of spectral images is likely to degrade spatial resolution and may also reduce the ability to perform advanced reconstruction algorithms such as compressed sensing [13].

#### 4. Application to nanoparticle samples

The time-dependent acquisition scheme illustrated in Fig. 8 has been successfully applied to produce tomographic reconstructions for AgAu nanoparticles. The projections of Au L $\alpha$  and Ag L $\alpha$  are shown in Fig. 10(i–ii) at tilt angles of  $-60^\circ$ ,  $0^\circ$  and  $60^\circ$ . The spectra from the full spectrum images at each of these tilt angles is also displayed in Fig. 10(iii).

Fig. 11 shows orthoslices and a volume render for one of these reconstructions, demonstrating the segregation of Ag to the surface at a composition of 60 at% Ag and 40 at% Au. A discussion of the correlation between compositional segregation and catalytic activity for this system can be found in Slater et al. [17]. The reconstructions here represent counts from only one peak in each case (Au L $\alpha$  and Ag L $\alpha$ ) but the counting statistics could be improved by using the full family of peaks. However, care should be taken to avoid overlapping peaks, as is the case for a number of peaks in the Au M and Ag L families in this case.

Previous studies have also successfully applied a standard ‘constant time’ acquisition approach to successfully reconstruct similar AgAu nanoparticles [29] as well as other nanoparticle systems [11,30]. However, there has been little discussion of the ability of the EDX signal intensity to satisfy the projection requirement.

##### 4.1. Projection requirement

The projection requirement of tomography states that the intensity of the signal used to perform the reconstruction must be a monotonic function of the quantity to be reconstructed [31], and direct proportionality between intensity and the physical quantity is desirable. A key question for EDX tomography is therefore whether the characteristic X-ray intensity generated in the STEM meets this requirement for the constraints of a particular sample and detector geometry.

The intensity of the characteristic X-ray signal for element A is related to the probability of ionisation. Where  $n_A$  is the number density of atoms of element A within the sample,  $Q_A$  is the ionisation cross section and  $t$  is the sample thickness, the probability of ionisation for an atom of element A is given by the product  $n_A Q_A t$ .

The expected characteristic X-ray generation can then be calculated by consideration of the competition between X-ray emission and other de-excitation methods, such as Auger electron emission, defined as the fluorescence yield ( $\omega_A$ ) [18]. The intensity of the X-ray signal for a specific characteristic X-ray of element A ( $I_A$ ) is therefore given by:

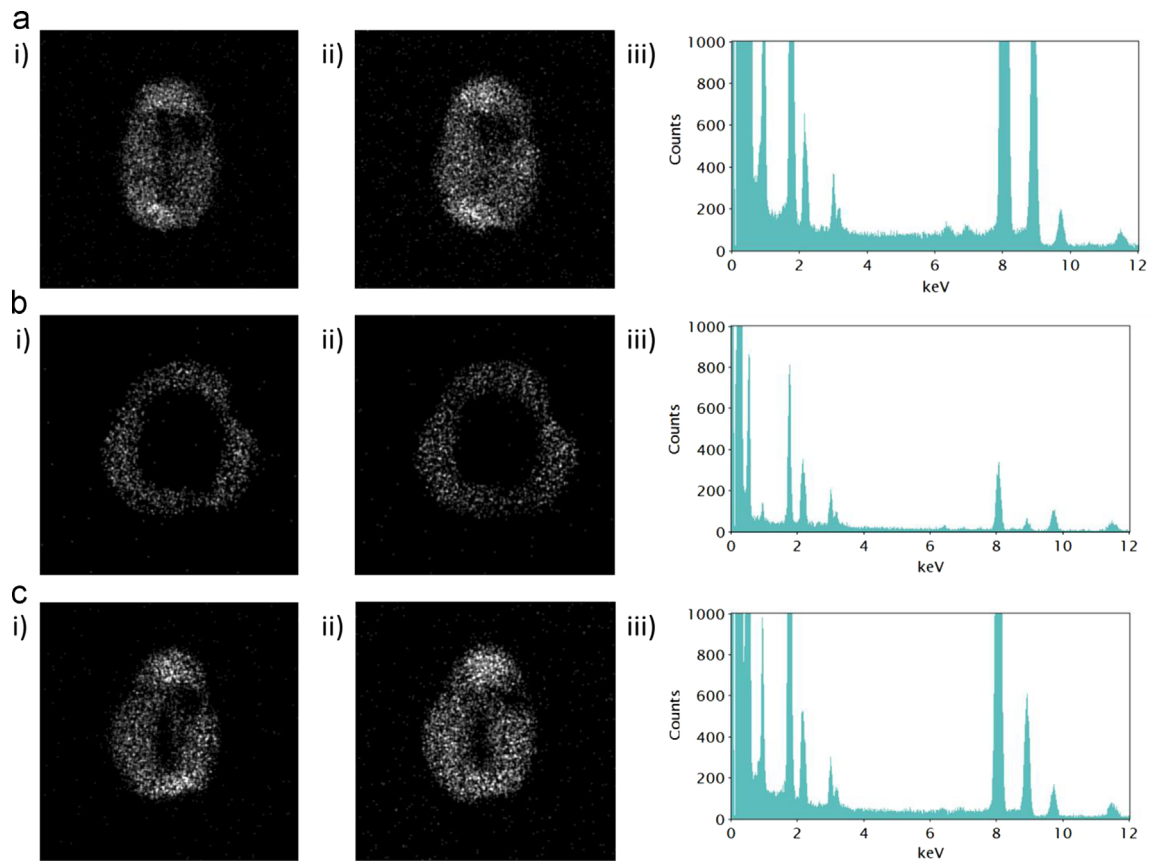


**Fig. 10.** Projections at (a)  $-60^\circ$ , (b)  $0^\circ$  and (c)  $60^\circ$  for (i) Au L $\alpha$  counts and (ii) Ag L $\alpha$  counts. (iii) Spectra from the full spectrum images at (a)  $-60^\circ$ , (b)  $0^\circ$  and (c)  $60^\circ$ .

$$I_A = n_A Q_A t \omega_A a_A D_e \left( \frac{\Omega}{4\pi} \right) \varepsilon_A \quad (3)$$

where  $a_A$  is the relative transition probability,  $D_e$  is the total number of electrons incident on the sample,  $\Omega$  is the detector solid angle and  $\varepsilon_A$  is the detector efficiency.

The only quantities in Eq. (3) which vary as a function of the two dimensional position within a spectrum image are the

number density of atoms of element  $A$  ( $n_A$ ) and the thickness of the sample. The intensity of the characteristic X-rays described in Eq. (3) therefore fully satisfies the projection requirement; the detected signal is directly proportional to the mass-thickness of element  $A$ . The exception to this is when crystals are oriented with the electron beam passing along a major zone-axis, resulting in the electron beam being more tightly bound to atomic columns due to electron channelling [27]. For this reason, a quantitative analysis

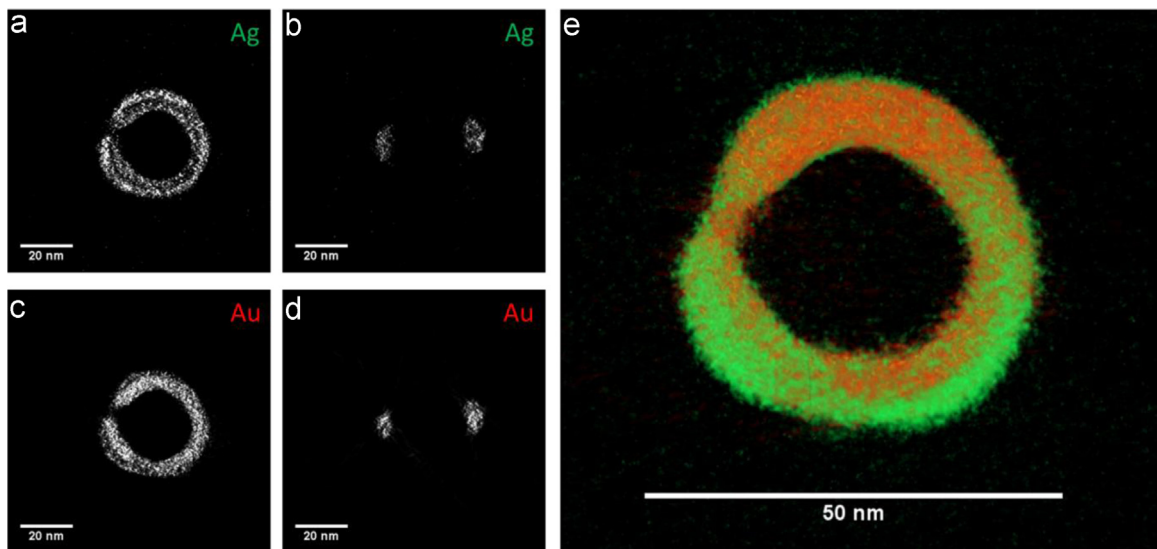


**Fig. 11.** Example of a tomographic reconstruction using a time-dependent acquisition scheme performed for a AgAu nanoparticle. (a) Orthoslice through the Ag reconstruction normal to the optic axis, displaying clear segregation of Ag to the surface of the nanoparticle. (b) Orthoslice through the Ag reconstruction parallel to the optic axis. (c) Orthoslice through the Au reconstruction normal to the optic axis. (d) Orthoslice through the Au reconstruction parallel to the optic axis. (e) Volume rendering of the Ag and Au reconstructions, Ag volume is green and Au volume is red.

should avoid channelling conditions or exclude projections of crystals close to major zone axes from reconstructions.

X-rays are produced not only through emission of characteristic X-rays from atoms within the sample but also through the deceleration of the electron beam in the sample. Bremsstrahlung, or ‘braking radiation’, is emitted as a continuous spectrum of X-rays that decreases in intensity with an increase in emitted X-ray energy. A sufficient signal-to-background ratio at each pixel allows subtraction of the Bremsstrahlung background through either background modelling or a simple two-window method [18]. If background subtraction is not performed, the contribution of Bremsstrahlung will affect the intensity of elemental maps produced at each tilt angle and therefore potentially influence the final tomographic reconstruction. The Bremsstrahlung signal scales proportionally with atomic number,  $Z$ , and therefore could cause several artefacts. For example, low energy X-rays may contain erroneous intensity in regions of high  $Z$ . For reconstruction of high energy X-ray peaks the Bremsstrahlung background is low and the contribution of Bremsstrahlung X-rays is not likely to significantly affect reconstructions.

#### 4.2. X-ray absorption

Eq. (3) also neglects the effect that X-ray absorption and fluorescence within the sample will have on the intensity of characteristic X-rays emitted. Here, we will consider the implications that absorption will have on the projection requirement. For absorption to negatively affect the ability of the sample to accurately satisfy the projection requirement, the absorption must vary across the spectrum image. The absorption of X-rays is described by an exponential attenuation law [18]:

$$I = I_0 e^{-\rho L \left(\frac{\mu}{\rho}\right)} \quad (4)$$

where  $I/I_0$  is the fraction of X-rays not absorbed at a particular energy,  $\rho$  is the density of the element and  $\left(\frac{\mu}{\rho}\right)$  is the mass attenuation coefficient of the element. Eq. (4) can be rearranged to calculate a maximum path length through the sample,  $L$ , for a fixed amount of absorption at a specific X-ray energy:

$$L = \frac{\ln \frac{I_0}{I}}{\rho \left(\frac{\mu}{\rho}\right)} \quad (5)$$

Fig. 12 uses elemental mass attenuation coefficients and standard specimen densities [32] to predict the maximum allowable X-ray path length for a single element sample as a function of atomic number in the limit of 1% absorption ( $I/I_0=0.99$ ) at two different X-ray energies (2 keV and 10 keV). This figure demonstrates that absorption is less than 1% and can safely be neglected for characteristic X-ray energies of 10 keV or above for a path length less than 50 nm and for an atomic number of less than 60. For less energetic X-rays (2 keV), a less stringent limit of 10% absorption ( $I/I_0=0.9$ ) yields similar acceptable sample constraints (specimen size less than 50 nm and atomic number less than 60). The values displayed in Fig. 12 provide a guide to understanding the size of specimens acceptable for EDX tomography and which X-ray energies are likely to provide elemental maps that most accurately satisfy the projection requirement.

Taking a 1% absorption limit, pure elemental Ag has a maximum allowable path length through the specimen of 80 nm for 10 keV X-rays and 7 nm for 2 keV X-rays. The same absorption limit for pure elemental Au gives a maximum path length through the specimen of 44 nm for 10 keV X-rays and 5 nm for 2 keV X-rays. In this study we focus on bimetallic AgAu nanoparticles with diameters of approximately 40 nm (Fig. 11), although the hollow morphology of the particles means that for most particles

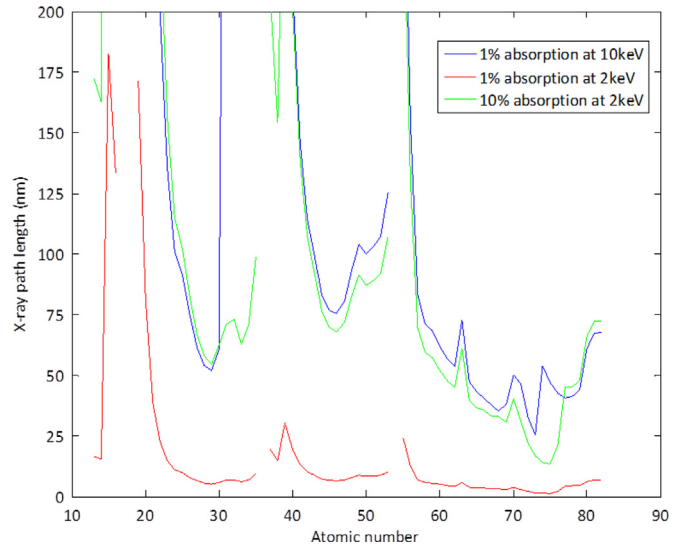


**Fig. 12.** Maximum X-ray path length in a sample as a function of atomic number for a single element sample when considering a limit of 1% absorption ( $I/I_0=0.99$ ) at two different X-ray energies (red, 2 keV and blue, 10 keV) and for a less stringent 10% absorption limit ( $I/I_0=0.9$ ) for an X-ray energy of 10 keV (green). Mass attenuation coefficients and the densities of elements used to calculate this data have been taken from NIST [32]. (For interpretation of the references to color in this figure legend, the reader is referred to the web version of this article.)

the maximum projected thickness is in practise typically 10 nm or less. For the AgAu nanoparticle used in this study (Fig. 11), the particle is roughly 50 at% of each element and the maximum X-ray path length is approximately 5 nm. The attenuation coefficient of mixtures and compounds can be obtained additively by:

$$\frac{\mu}{\rho} = \sum_i w_i \left(\frac{\mu}{\rho}\right)_i \quad (6)$$

where  $w_i$  is the weight fraction of the  $i$ th atomic constituent [33]. Absorption of 2 keV X-rays through the nanoparticle of interest (Fig. 11) was found to be at maximum 1%, validating the use of X-ray peaks above 2 keV in the reconstruction of this nanoparticle (Au  $M\alpha=2.1$  keV). However, 1 keV X-rays will undergo maximum absorption of approximately 4% within the nanoparticle which suggests that carbon (0.277 keV) and oxygen (0.525 keV)  $K\alpha$  X-rays will show significant variations in absorption even in this small sample. The use of a maximum path length differs from standard absorption correction procedures [34] which integrate the X-ray path lengths along the electron beam within the sample. The complex geometry of these particles makes integration challenging and hence we choose to consider the maximum path length as this will provide an overestimate to X-ray absorption within an image and so a conservative estimate of thickness.

#### 4.3. Variations in detector shadowing across a sample area

Another possible violation of the projection requirement comes from the fact that the extent of detector shadowing varies as a function of sample position, and consequently it is feasible for shadowing to vary within a single spectrum image. This situation is illustrated in Fig. 13 which shows a 2D cross-section subtending the sample, the shadowing object and the middle of a single Super-X detector (top right). The difference in angle,  $\Delta\theta$ , at which X-rays are shadowed for two points at the extremes of the spectrum image (separated by a distance  $\Delta l$ ), due to the presence of an object with height  $H$  (typically the holder or grid bars) at a distance  $l$  from the image area is calculated geometrically as:

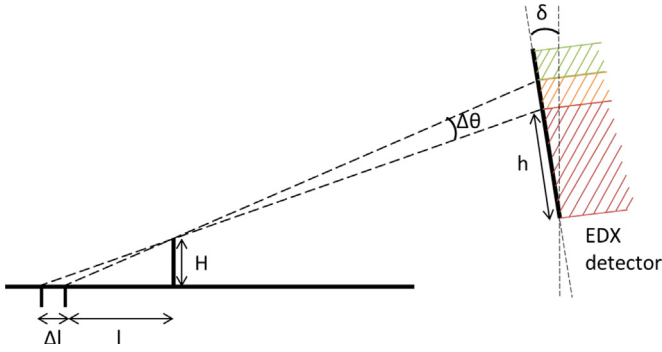


**Fig. 13.** Diagram illustrating the variation in detector shadowing between two points on the sample separated by a distance  $\Delta l$ , shadowed by an object of height  $H$  at a distance  $l$  from the image area. (For interpretation of the references to color in this figure legend, the reader is referred to the web version of this article.)

$$\Delta\theta = \tan^{-1}\left(\frac{H}{l}\right) - \tan^{-1}\left(\frac{H}{l+\Delta l}\right). \quad (7)$$

Using geometrical calculations an order of magnitude estimate of the variation of shadowing across an EDX spectrum image area can be estimated as a function of  $\alpha$ -tilt. We use the variation in the unshadowed detector area as an estimate of the variation in X-ray counts across an image area. This is an approximation that does not take in to account the change in X-ray flux density across the detector but provides an accurate order of magnitude estimate. The detector area,  $A$ , shadowed by an object casting a shadow of height  $h$  on the detector, which is a function of  $\theta_T$ , the polar angle due to tilt of the sample, is given by

$$A(\theta_T) = r^2 \cos^{-1}\left(\frac{r - h(\theta_T)}{r}\right) - (r - h(\theta_T))\sqrt{2rh(\theta_T) - h(\theta_T)^2} \quad (8)$$

where  $r$  is the radius of the detector.

For the Super-X detector system the variation in shadowing for each pair of detectors (1+2 or 3+4 as shown in Fig. 1a) must be considered separately but, *within* a pair, the shadowing can be assumed to behave identically, due to their equivalent position with respect to the  $\alpha$ -tilt axis. The proportion of the detector area that is partially shadowed across the image, compared to the detector area that is entirely unshadowed is termed  $P_{12}$  for detector pair 1+2 and  $P_{34}$  for detector pair 3+4.

We begin by discussing the shadowing resulting from the top side of the sample holder, for the situation where both pairs of

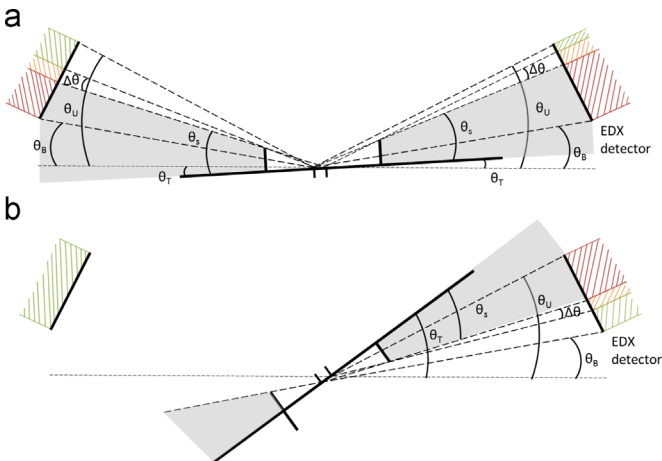


**Fig. 14.** Diagram illustrating the geometry of angles used in determination of the extent of detector shadowing from (a) the top side of the sample holder and (b) the bottom side of sample holder (grid bars).

detectors are partially shadowed simultaneously (Fig. 14a). From simple trigonometry the height,  $h$ , of the shadow cast upon the detector is given by

$$h = d \sec(\theta_E - \theta_B) \sin(\theta_S + \theta_T - \theta_B) \sec(\theta_S + \theta_T - \delta) \quad (9)$$

where  $d$  is the distance to the centre of the detectors from the sample,  $\theta_E$  is the elevation angle of all detectors (assumed to be the same),  $\theta_B$  is the angle to the bottom of the detector pair,  $\theta_S$  is the angle over which the object shadows the detector pair, and  $\delta$  is the polar tilt angle of the detector. All angles are defined in the plane of the sample and two Super-X detectors (at a  $45^\circ$  azimuthal angle to the  $\alpha$ -tilt axis) as show in Fig. 14a. An  $\alpha$ -tilt of the sample can be translated to a polar tilt angle  $\theta_T$ , as  $\theta_T = \tan^{-1}(\tan\alpha\cos45)$ .

In the range of tilt angles in which detector shadowing from the top of the sample holders occurs  $P_{12}$  and  $P_{34}$  are defined as

$$P_{12} = \frac{A(-\theta_T + \Delta\theta) - A(-\theta_T)}{A(-\theta_T + \Delta\theta)} \text{ between } -\theta_T + \theta_S + \Delta\theta = \theta_U \text{ and } -\theta_T + \theta_S = \theta_B \quad (10)$$

$$\text{and } P_{34} = \frac{A(\theta_T - \Delta\theta) - A(\theta_T)}{A(\theta_T - \Delta\theta)} \text{ between } \theta_T + \theta_S + \Delta\theta = \theta_U \text{ and } \theta_T + \theta_S = \theta_B \quad (11)$$

Eqs. (10) and (11) provide the variation in shadowing when using only one detector pair, either detectors 1 and 2 or detectors 3 and 4. The variation in shadowing can reach 100% across the image area when the detector pair is fully shadowed at one side of the area, i.e.  $P_{12}=1$  when  $\Delta\theta = \theta_U - \theta_S + \theta_T$  and  $P_{34}=1$  when  $\Delta\theta = \theta_U - \theta_S - \theta_T$ . For this reason, when using a detector located only on one side of the tilt axis, care should be taken to avoid acquiring tomographic data for tilt angles close to this maximum shadowing condition.

However, when both detector pairs are used, as is the case in this study, the shadowing effect is largely mitigated by the greater effective detector area provided by the complementary detector pair on the other side of the tilt axis. To calculate the contribution from both detectors we have to multiply the variation in shadowing of a single detector pair  $P_{ij}$  by the angular fraction of the total detector area that this detector pair is subtending  $Q_{ij}$ . This value is given by

$$Q_{12} = \frac{A(-\theta_T + \Delta\theta)}{A(-\theta_T + \Delta\theta) + A(\theta_T - \Delta\theta)} \text{ and } Q_{34} = \frac{A(\theta_T - \Delta\theta)}{A(-\theta_T + \Delta\theta) + A(\theta_T - \Delta\theta)} \quad (12)$$

Thus, the maximum variation in shadowing across the specimen distance  $\Delta l$  when considering all detectors,  $P$ , can then be expressed as a percentage,

$$P = 100 \times (P_{12} \times Q_{12} - P_{34} \times Q_{34}) \quad (13)$$

$$\text{or } P = 100 \times \left( \frac{(A(-\theta_T + \Delta\theta) - A(-\theta_T)) - (A(\theta_T - \Delta\theta) - A(\theta_T))}{A(-\theta_T + \Delta\theta) + A(\theta_T - \Delta\theta)} \right) \quad (14)$$

We have determined the corresponding angles approximately from our tilt-series data (Fig. 2b) and from the optical data of the sample holder (Fig. 3). Fitting a Gaussian to our experimental tilt-series data in Fig. 2b reveals an average minimum in counts at an  $\alpha$ -tilt of approximately  $18^\circ$ , equivalent to a polar angle of  $\theta_T = 13^\circ$ , which we have related to the elevation angle of all four detectors. We have used a detector tilt of  $\delta = 0-15^\circ$  and note that this has little effect on our calculations, with no change in shadowing variation to 1 significant figure. The angles  $\theta_U$  and  $\theta_B$  are determined from the elevation angle, tilt and radius of the detectors.

From the optical profile data (Fig. 3) we know that on the top side of the sample holder the height of the shadowing is  $h=600\ \mu\text{m}$  and the distance to the shadowing is  $l=1.6\ \text{mm}$ , from which we calculate values of  $\theta_S=21^\circ$  and  $\Delta\theta=0.001^\circ$  when  $\Delta l=100\ \text{nm}$ . Note in this and subsequent equations we have also tacitly assumed that there are no contributions to this shadowing from any collimators, which are absent in our system. However, for different configurations, should collimators be present, then their presence will slightly modify the preceding equations which are based purely on the effective radius of the detector.

Using these values, over a distance of 100 nm the percent of shadowing due to the top side of the holder reaches a maximum of  $3 \times 10^{-3}\%$ .  $P_{12}$  and  $P_{34}$  will have opposite signs, meaning the variation in shadowing is in the opposite direction for each detector pairs and acts to somewhat compensate the detector shadowing from each detector pair.

Considering shadowing from the underside of the sample the shadowing height,  $h$ , on the detector is given by

$$h = d \sec(\theta_U - \theta_E) \sin(\theta_U + \theta_S - \theta_T) \sec(\theta_S - \theta_T + \delta) \quad (15)$$

On the underside of the sample grid, our optical measurements have demonstrated that the sample only causes shadowing for a polar angle of less than  $18^\circ$ , while the middle of a grid square to the height of the grid bars in the TEM grids used in this study was  $24^\circ$ . This suggests that the maximum shadowing angle on the underside of the sample is due to the grid bars ( $\theta_S=24^\circ$ ), as shown in Fig. 4. However, bowing of the carbon film across a grid square could lead to an increase or decrease in this angle. Assuming the carbon film lays flat, shadowing due to grid bars can be estimated using values of width and depth obtained from suppliers in each particular case, or through measurement of grid dimensions. In this case, we have used grids with a hole of width  $90\ \mu\text{m}$  and a grid bar depth of  $20\ \mu\text{m}$ . Assuming the sample area is located in the middle of a grid square, the angular difference between points 100 nm from each other gives  $\Delta\theta=0.05^\circ$ . For the underside of the sample  $P_{12}$  and  $P_{34}$  are calculated in a similar manner to the top side of the sample holder:

$$P_{12} = \frac{A(-\theta_T + \Delta\theta) - A(-\theta_T)}{A(-\theta_T + \Delta\theta)} \text{ between } -\theta_T + \theta_S + \Delta\theta = \theta_U$$

and  $-\theta_T + \theta_S = \theta_B$  (16)

$$\text{and } P_{34} = \frac{A(\theta_T - \Delta\theta) - A(\theta_T)}{A(\theta_T - \Delta\theta)} \text{ between } \theta_T - \theta_S = \theta_U$$

and  $\theta_T + \theta_S - \Delta\theta = \theta_B$ . (17)

However, unlike for the top side of the specimen holder both detector pairs are never simultaneously shadowed (Fig. 14b) and therefore the variation in shadowing can be given simply by

$$P = 100 \times \left( \frac{A(-\theta_T + \Delta\theta) - A(-\theta_T)}{A(-\theta_T + \Delta\theta) + 1} \right) \quad (18)$$

This reaches a maximum of 0.1% and hence can be largely ignored for high spatial resolution tomographic data sets. Importantly, for larger image areas, images taken close to the grid bars or for grids with smaller grid areas this variation may be large enough so that projections at a number of angles should be removed from the tilt series. For instance, if the nanoparticle was located at a  $10\ \mu\text{m}$  distance to the grid bars closest to detectors 1 and 2, as represented by the red dot in Fig. 5b, the shadowing angle due to grid bars would increase to  $\theta_S=63^\circ$ , increasing  $\Delta\theta$  to  $0.2^\circ$  over a 100 nm image area. In this case the variation in shadowing across the image area would reach approximately 30%. Care should always be taken to ensure that the sample is situated away from any grid bars when using a

standard TEM grid and the use of fine-mesh grid entirely avoided. In fact, the use of continuous films may be preferable to entirely remove the contribution of grid bars to shadowing. We further note that where data is acquired from specimen areas close to the grid bars or from a grid with a smaller mesh size the shadowing from the top side may also be due to grid bars rather than the sides of the sample holder.

## 5. Conclusions

New designs of large solid angle energy dispersive X-ray detector systems using multiple detectors have made EDX tomography more readily accessible. However, careful consideration of sample and acquisition parameters is required to optimise data acquisition schemes and to ensure that artefacts associated with low signal-to-noise ratio data do not affect the fidelity of reconstructions. We have proposed a novel time-varied acquisition scheme that compensates the effect of detector shadowing for the Titan's Super-X EDX system, maximising the available X-ray signal when using a penumbra-limited single-tilt tomography holder. This compensated acquisition scheme provides approximately constant X-ray counts in the characteristic peaks over the full range of specimen tilt angles.

The intensity of reconstructions in EDX tomography, without considering absorption of X-rays, is directly proportional to the number of atoms per unit volume of the element in question. Absorption of X-rays limits the size of samples in which this proportionality holds true and, at some thickness of sample, absorption will result in violation of the projection requirement, particularly for high atomic number samples and reconstructions of low energy X-ray signals. We have considered the potential for shadowing variations within a single spectrum image field of view and determine that these are insignificant and can be largely ignored for small sample areas ( $< 100\ \text{nm}$ ) when using all four Super-X EDX detectors.

## Acknowledgements

S.J.H. and T.J.A.S. acknowledge funding from multiple research grants including the Engineering and Physical Sciences Research Council (EPSRC) UK Grants EP/G035954/1 and EP/J021172/1 and Defence Threat Reduction Agency Grant HDTRA1-12-1-0013. T.J.A.S. would like to thank the North West Nanoscience Doctoral Training Centre (NOWNano DTC) for supporting his work. N.J.Z. also acknowledges support from the Electron Microscopy Center at the Center for Nanoscale Materials of Argonne National Laboratory, a U. S. Department of Energy, Office of Science, Office of Basic Energy Sciences User Facility under Contract no. DE-AC02-06CH11357, as well as, a visiting appointment in the School of Materials at the University of Manchester. The authors wish to acknowledge the support from HM Government (UK) for the provision of the funds for the FEI Titan G2 80-200 S/TEM associated with research capability of the Nuclear Advanced Manufacturing Research Centre.

## References

- [1] P.A. Midgley, R.E. Dunin-Borkowski, Electron tomography and holography in materials science, *Nat. Mater.* 8 (2009) 271–280.
- [2] S. Bals, B. Goris, L.M. Liz-Marzan, G. Van Tendeloo, Three-Dimensional characterization of noble-metal nanoparticles and their assemblies by electron tomography, *Angew. Chem. Int. Ed.* 53 (2014) 10600–10610.
- [3] L.C. Gontard, R.E. Dunin-Borkowski, D. Ozkaya, Three-dimensional shapes and spatial distributions of Pt and PtCr catalyst nanoparticles on carbon black, *J. Microsc.* 232 (2008) 248–259.
- [4] S. Sueda, K. Yoshida, N. Tanaka, Quantification of metallic nanoparticle morphology on  $\text{TiO}_2$  using HAADF-STEM tomography, *Ultramicroscopy* 110 (2010)

- 1120–1127.
- [5] J.C. Hernandez-Garrido, et al., The location of gold nanoparticles on titania: A study by high resolution aberration-corrected electron microscopy and 3D electron tomography, *Catal. Today* 160 (2011) 165–169.
- [6] R.F. Klie, I. Arslan, N.D. Browning, Atomic resolution electron energy-loss spectroscopy, *J. Electron. Spectrosc.* 143 (2005) 105–115.
- [7] A.J. D'Alfonso, B. Freitag, D. Klenov, L.J. Allen, Atomic-resolution chemical mapping using energy-dispersive x-ray spectroscopy, *Phys. Rev. B* 81 (2010) 100101.
- [8] G. Mobus, R.C. Doole, B.J. Inkson, Spectroscopic electron tomography, *Ultramicroscopy* 96 (2003) 433–451.
- [9] N.J. Zaluzec, Innovative instrumentation for analysis of nanoparticles: the  $\pi$  Steradian detector, *Microsc. Today* 17 (2009) 56–59.
- [10] P.J. Phillips, et al., A new silicon drift detector for high spatial resolution STEM-XEDS: performance and applications, *Microsc. Microanal.* 20 (2014) 1046–1052.
- [11] A. Genc, et al., XEDS STEM tomography for 3D chemical characterization of nanoscale particles, *Ultramicroscopy* 131 (2013) 24–32.
- [12] K. Lepinay, F. Lorut, R. Pantel, T. Epicier, Chemical 3D tomography of 28 nm high K metal gate transistor: STEM XEDS experimental method and results, *Micron* 47 (2013) 43–49.
- [13] R. Leary, Z. Saghi, P.A. Midgley, D.J. Holland, Compressed sensing electron tomography, *Ultramicroscopy* 131 (2013) 70–91.
- [14] B. Goris, T. Roelandts, K.J. Batenburg, H. Heidari Mezerji, S. Bals, Advanced reconstruction algorithms for electron tomography: from comparison to combination, *Ultramicroscopy* 127 (2013) 40–47.
- [15] H.S. von Harrach, et al., An integrated silicon drift detector system for FEI Schottky field emission transmission electron microscopes, *Microsc. Microanal.* 15 (2009) 208–209.
- [16] T.J.A. Slater, P.H.C. Camargo, M.G. Burke, N.J. Zaluzec, S.J. Haigh, Understanding the limitations of the Super-X energy dispersive X-ray spectrometer as a function of specimen tilt angle for tomographic data acquisition in the S/TEM, *J. Phys. Conf. Ser.* 522 (2014) 012025.
- [17] T.J.A. Slater, et al., Correlating catalytic activity of Ag–Au nanoparticles with 3D compositional variations, *Nano Lett.* (2014) 1921–1926.
- [18] D.B. Williams, C.B. Carter, *Transmission Electron Microscopy*, second ed., Springer, New York, 2009.
- [19] W.S. Rasband, *ImageJ*, U.S. National Institutes of Health, Bethesda, Maryland, USA, 1997–2014.
- [20] M.V. Petri, R.A. Ando, P.H.C. Camargo, Tailoring the structure, composition, optical properties and catalytic activity of Ag–Au nanoparticles by the galvanic replacement reaction, *Chem. Phys. Lett.* 531 (2012) 188–192.
- [21] N.J. Zaluzec, Analytical formulae for calculation of X-ray detector solid angles in the scanning and scanning/transmission analytical electron microscope, *Microsc. Microanal.* 20 (2014) 1318–1326.
- [22] C.S.M. Yeoh, et al., The dark side of EDX tomography: modeling detector shadowing to aid 3D elemental signal analysis, *Microsc. Microanal. FirstView* (2015) 1–6.
- [23] P. Schlossmacher, D. Klenov, B. Freitag, H.S. von Harrach, Enhanced detection sensitivity with a new windowless XEDS system for AEM based on silicon drift detector technology, *Microsc. Today* 18 (2010) 14–20.
- [24] J.M. Thomas, et al., The chemical application of high-resolution electron tomography: bright field or dark field? *Angew. Chem. Int. Ed.* 43 (2004) 6745–6747.
- [25] K.J. Batenburg, et al., 3D imaging of nanomaterials by discrete tomography, *Ultramicroscopy* 109 (2009) 730–740.
- [26] J. Frank, S. Brandt, *Electron Tomography*, second ed., Springer, New York, 2008.
- [27] P. Kotula, L. Brewer, J. Michael, L. Giannuzzi, Computed tomographic spectral imaging: 3D STEM-EDS spectral imaging, *Microsc. Microanal.* 13 (2007) 1324–1325.
- [28] T. Yaguchi, M. Konno, T. Kamino, M. Watanabe, Observation of three-dimensional elemental distributions of a Si device using a 360°-tilt FIB and the cold field-emission STEM system, *Ultramicroscopy* 108 (2008) 1603–1615.
- [29] B. Goris, L. Polavarapu, S. Bals, G. Van Tendeloo, L.M. Liz-Marzan, Monitoring galvanic replacement through three-dimensional morphological and chemical mapping, *Nano Lett.* 14 (2014) 3220–3226.
- [30] N. Liakakos, et al., Co–Fe nanodumbbells: synthesis, structure, and magnetic properties, *Nano Lett.* 14 (2014) 2747–2754.
- [31] P.B. Hirsch, M.J. Whelan, A. Howie, On production of X-rays in thin metal foils, *Philos. Mag.* 7 (1962) 2095.
- [32] S.M. Seltzer, J.H. Hubbell, Tables and Graphs of Photon Mass Attenuation Coefficient and Mass Energy-Absorption Coefficients for Photon Energies 1 keV to 20 MeV for Elements Z=1 to 92 and Some Dosimetric Materials, Appendix to invited plenary lecture by J.H. Hubbell "45 Years (1950–1995) with X-Ray Interactions and Applications" presented at the 51st National Meeting of the Japanese Society of Radiological Technology, Nagoya, Japan (1995).
- [33] S.M. Seltzer, Calculation of photon mass energy-transfer and mass energy-absorption coefficients, *Rad. Res.*, 136, (1993) 147–170.
- [34] J. Philibert, A method for calculating the absorption correction in electron-probe microanalysis, in: 3rd International Congress on X-ray Optics and Microanalysis, H.H. Pattee, V.E. Cosslett, A. Engstrom, (Eds.), p. 379.tp